Atmos. Meas. Tech. Discuss., https://doi.org/10.5194/amt-2018-319
Manuscript under review for journal Atmos. Meas. Tech.
Discussion started: 6 November 2018

Evaluation of microwave radiances of GPM/GMI for the all-sky assimilation in RTTOV framework

Rohit Mangla[1], Jayaluxmi Indu[1,2]

[1]Department of Civil Engineering, Indian Institute of Technology, Bombay, India
[2]Interdisciplinary Center for Climate Studies, Indian Institute of Technology Bombay, India
Correspondence to: Jayaluxmi Indu (indusj@civil.iitb.ac.in)

Abstract. This study evaluates the all-sky GPM/GMI radiances towards assimilation in regional mesoscale model at 183±7 GHz. The radiative transfer model (RTM) namely RTTOV-SCATT is used for the simulation of three tropical cyclones (hudhud, vardah and kyant respectively). Within the RTM, the performance of non-spherical Discrete Dipole Approximation (DDA) shapes (sector snowflake, 6-bullet rosette, block-column and thinplate) are evaluated. The input data used in RTTOV-SCATT includes vertical hydrometeor profiles, humidity and surface fluxes. In addition, the first guess simulations from Weather Research Forecast (WRF) model were executed at 15 km resolution using ERA-Interim reanalysis datasets. Results indicate that observed minus first guess (FG departures) are symmetric with DDA shapes. The normalized probability density function of FG departures shows large number of spatially correlated samples between clear-sky and poorly forecasted region. Quality control (QC) method was performed to eliminate large FG departures due to instrumental anomalies or poor forecast of clouds and precipitation. The goodness of fit test, h-statistics and skewness of observed and simulated distribution show optimum results for thinplate shape in all the convective events. We also tested the high resolution ERA-5 reanalysis datasets for the simulation of all-sky radiances using thinplate shape. Results illustrate a potential to integrate the GMI sensor data within a WRF data assimilation system.

Atmos. Meas. Tech. Discuss., https://doi.org/10.5194/amt-2018-319
Manuscript under review for journal Atmos. Meas. Tech.
Discussion started: 6 November 2018

Atmospheric Measurement Techniques Discussions

1 Introduction

The Numerical weather prediction (NWP) model is widely used for forecasting the evolution of the surface and atmospheric conditions. To predict the state of the atmosphere, the NWP model relies on mathematical models and best initial conditions of the state of the atmosphere. Even though NWP models provide meaningful forecasts, they are biased owing to model structure and approximation of subgrid-scale processes (Shastri et al., 2017). In addition, it is also challenging to define the best initial conditions of the atmosphere state. Recent developments by operational NWP centers state that assimilating satellite radiances improves the forecast skills (Islam et al., 2016; Routray et al., 2016; Saunders et al., 2013; Singh et al., 2016). Studies show that assimilation of all-sky (clear and cloudy) microwave radiances in global NWP models have a large positive impact on temperature and humidity (Geer, 2013; Kazumori et al., 2014; Lean et al., 2017). The satellite radiances from microwave imagers [Tropical Rainfall Measuring Mission (TRMM) microwave imager (TMI) (Kummerow et al., 1998), Aqua Advanced microwave scanning radiometer for earth observing system (Kawanishi et al., 2003), Advanced Microwave Scanning Radiometer-2 (AMSR-2) (JAXA, 2013), Special Sensor Microwave Imager Sounder (SSMIS) (Kunkee et al., 2008) and Global Precipitation Measurement (GPM) Microwave Imager (GMI) (Hou et al., 2014)] contain crucial information on deep and intense convection (Otkin, 2012).

Study of rainfall/convective systems involve examining the naturally emitted electromagnetic radiation from the earth which interacts with atmospheric gases like water vapour, hydrometeors (precipitation-sized particles of rainfall, snowfall, ice crystals etc). A radiative transfer model (RTM) uses profiles of all the observed variables to provide the satellite observations which can be either brightness temperature (Tb) (from radiometer) or reflectivity (from radar). An accurate comparison between model and observed forecast relies strongly on the assumptions used for radiation-hydrometeor interaction. To generate improved initial conditions of the model, a crucial role is played by the assumptions made when simulating observations from different instruments in space. To date, the scientific community has not really examined this important aspect.

Existing studies state that within the microwave frequency ranges (10-183 GHz), assuming spherical shapes for snow/ice particles in RTM models produce un-realistic scattering in deep convective clouds (Hong et al., 2005). Geer and Baordo, (2014) introduced the realistic 3D discrete dipole approximation (DDA) non-spherical shapes to represent frozen hydrometeors within an

Atmos. Meas. Tech. Discuss., https://doi.org/10.5194/amt-2018-319
Manuscript under review for journal Atmos. Meas. Tech.
Discussion started: 6 November 2018

Atmospheric Measurement Techniques Discussions
Open Access
EGU

RTM model. The DDA shapes examined are usually long column, short column, block column, thick plate, thin plate, 3,4,5 and 6 bullet rosette, sector and dendrite snowflake shapes (Liu, 2008). Geer and Baordo, (2014) claimed that DDA sector snowflake is approximately fit for all frequencies at a global scale but it doesn't perform well at the regional level. Regional case studies show that block column over Indian ocean (Guerbette et al., 2016) and thinplate over Mediterranean region (Rysman et al., 2016) have improved the simulation of low Tb at convective scale for 183 GHz. Hence, careful investigation of DDA shapes is required at the regional level, prior the simulation of cloudy radiances at a higher frequency. Generally, the best choice of DDA shapes at each frequency is based on the statistical analysis of the FG departures which is important in variational data assimilation techniques (Fowler and Van Leeuwen, 2013). Assimilation of satellite radiances offer difficulty due to cloud processes that non-linearly affect the upwelling radiations, non-gaussian FG departures statistics and systematic biases from NWP and radiative transfer models (RTM) (Errico et al., 2007; Okamoto, 2017).

The issue of non-gaussian characteristics of FG departure could be resolved using cloud dependent standard deviation (SD_{cloud}) (Geer and Bauer, 2011; Okamoto, 2017; Okamoto et al., 2014). The study conducted by Geer and Bauer, (2011) proposed a symmetric error model between SD_{cloud} and cloud amount predictor for all-sky microwave observations. The authors used the error model for AMSR-E observations at 19 GHz and observed that the probability distribution function (pdf) of normalized FG departures follow a gaussian distribution if normalization is done by SD_{cloud}. Geer, (2013) used the same model at multiple frequencies of TMI and SSMIS channel. In microwave spectrum, the symmetric error model is known to perform well for low frequencies (<50 GHz) as low frequencies are sensitive to cloud liquid droplets and rain-drops (Skofronick-Jackson and Wang, 2000) for which the particle shape and density are pre-defined. At higher microwave frequencies, the backscatter/brightness temperature registered by the sensor is mainly due to scattering from frozen hydrometeors, assuming a spherical shape (Geer and Baordo, 2014). Long-term monitoring of FG departure was found useful for identifying the instrumental error from ground based microwave observation (De Angelis et al., 2017).

This study investigates the simulation of all-sky GMI radiances of tropical cyclones over Indian region at 183 ± 7 GHz. In the analysis, we examined the cloud effect to evaluate the normalized FG departures. For the appropriate selection of DDA shapes, we inspect the statistical measure of

FG departures. In addition, we also include the analysis of ERA-5 reanalysis datasets (Malardel et al., 2015) to extend the sensitivity to cloud physical processes at a higher resolution. Section 2 briefly summarizes the GMI radiance datasets, NWP and RTM experimental setup. The simulation results and error analysis are demonstrated in section 3. Summary and conclusions are provided in section 4.

2 Data and Methods

2.1 GPM/GMI observations

The GMI sensor is a conically scanning passive radiometer on board the GPM satellite (Hou et al., 2014) developed by National Aeronautics and Space Administration (NASA) in collaboration with Japan Aerospace Exploration Agency (JAXA) and successfully launched on 28th February 2014. Being a successor of TRMM (Kummerow et al., 1998) the GPM mission has several advantages. GMI data is acquired in 13 channels in low (10-89 GHz) and high frequency (166-183 GHz) bands [Table 1] while TMI was limited to just 9 low-frequency bands. GMI has additional capabilities of detecting light precipitation and extending the global coverage to the mid-latitude region ($60^oS - 60^oN$). The horizontal resolution has been improved in GMI datasets because of the increase in reflector size of GMI (1.2 m) from TMI (61 cm). Figure 1 shows hudhud cyclone event on 9th October 2014, 06 UTC at 10, 89 and 183±7 GHz frequency. The low frequency channel (10 GHz) is sensitive to only liquid precipitation and greatly affected by surface emissivity (Hou et al., 2014). The discrimination between land and ocean (Figure 1) is clear in 10 GHz, moderate in 89 GHz and insensitive at 183 GHz. Furthermore, 183 ± 7 GHz channel can investigate deeply the atmosphere and it is highly sensitive to frozen hydrometeors. This channel is moderately sensitive to rain and cloud liquid water and also detect the scattering signals from small ice particles (Bennartz and Bauer, 2003; Laviola and Levizzani, 2011). In Figure 1, a strong depression of temperature lower than 100 K can be seen over ocean at 183 ± 7 GHz indicating the presence of frozen hydrometeors in deep convection. For the present study, GMI level 1b radiances for three tropical cyclones at $183 \pm 7\ GHz$-V (hereafter band 13) is used.

Atmos. Meas. Tech. Discuss., https://doi.org/10.5194/amt-2018-319
Manuscript under review for journal Atmos. Meas. Tech.
Discussion started: 6 November 2018

2.2 RTTOV-SCATT v12.1 Model

The all-sky GMI radiances have been simulated using RTTOV-SCATT (version 12.1) of Radiative Transfer for the television infrared observation vertical sounder (RTToV) (Hocking et al., 2017; Saunders et al., 2017). The RTToV is initially developed by ECMWF which was then upgraded within the European Organization for the Exploitation of Metereological Satellites (EUMETSAT) NWP satellite application facility. This Model is suitable for rapid transformation of a huge number of NWP model outputs into the radiance space. The RTTOV-SCATT is a separate interface for the simulation of cloud and precipitation affected microwave radiances. As an input to RTTOV-SCATT model, the atmopheric profiles (i.e. temperature, water vapour, cloud liquid water, ice, snow and rain) were derived from WRF NWP model output. The delta-eddington approximation is used for solving the radiative transfer equations to simulate the scattering effects of clouds and precipitations (Joseph et al., 1976). The surface emissivity over oceans are calucated by the surface parameters (eg. Temperature, surface wind) using the microwave surface emissivity model (FASTEM-version 6) (Kazumori and English, 2015). The all-sky Tb computed represent the weighted summation of the clear and cloudy independent columns (eq. 1). The weighing criteria is decided by the cloud fraction (Geer et al., 2009) which is based upon the variation in cloud and precipitation at subgrid scale.

$$Tb^{all-sky} = C_f * Tb^{cloudy} + \left(1 - C_f\right) * Tb^{clear-sky} \quad (1)$$

Here, C_f represents the vertical profile of cloud fraction.

2.3 WRF NWP Model

The WRF is specifically designed for regional forecast in operational and research NWP centers (Skamarock et al., 2008). The present study used the version 3.8 of WRF model for the forecasting of tropical cyclones over Indian region. We designed the experimental setup in a single domain from $3^o N\ to\ 26^o N$ and from $73^o\ E\ to\ 103^o E$ with 213x165 horizontal grids of 15 km resolution [Figure 2 (a)]. This experiment is configured with 51 number of vertical layers and model top is at 125 hPa. The initial and boundary conditions are taken from ERA-Interim reanalysis datasets (product of ECMWF) with specification of 71 km spatial resolution at 6 h interval (Simmons et al., 2007). Geographical parameters including land use land cover (LULC), topography, soil type,

Atmos. Meas. Tech. Discuss., https://doi.org/10.5194/amt-2018-319
Manuscript under review for journal Atmos. Meas. Tech.
Discussion started: 6 November 2018

lake and vegetation parameters are provided by the United States Geological Survey (USGS) global datasets at 30 sec resolution. Three tropical cyclones named “Hudhud” (October7-14, 2014), “Vardah” (December 6-12, 2016) and “Kyant” (October 21-27, 2016) over Bay of Bengal (BOB) regions are considered in this study. Their tracks are shown in Figure 2 (b).

The physical parameterization schemes used are as suggested by (Routray et al., 2016) over BOB region are; WRF single moment 6-class microphysics scheme (Hong and Lim, 2006), Kain-Fritsch convection scheme (Kain, 2004), Yonsei scheme for planetary boundary layer (Hong et al., 2006), Dudhia shortwave radiation scheme (Dudhia, 1989), rapid radiative transfer model scheme for long-wave radiation (Mlawer et al., 1997) and Noah land surface model scheme (Tewari et al., 2004). This configuration is highly versatile for the prediction of short range forecast over the Indian region (Kumar et al., 2014; Singh et al., 2016).

3 Results and Discussion

In the present study, DDA shapes of sector snowflake is used as first step for intial error analysis in section 3.1-3.4 (Geer and Baordo, 2014). In section 3.5, a statistical investigation is conducted to identify the best shape among the recognized DDA shapes (i.e., Sector snowflake, thinplate, 6-bullet rosette and block-column). In this study, the density of hydrometeros (rain and cloud liquid water=1000 kg/m^3; ice=917 kg/m^3 ; snow= 50 kg/m^3) and particle size distributions by Field et al., (2007) for snow, marshall-palmer distribution for rain, modified-gamma distribution for cloud liquid water and cloud ice have been used.

3.1 Spatial Distribution of observed and simulated Tb

The Figure 3 shows comparison between the all-sky simulated radiances at band 13 with respect to the observed GMI radiances for three cyclonic events over the BOB region. The microwave observations were averaged to 15 km horizontal resolution to match closely with the effective resolution of NWP model. The increased scattering from frozen hydrometeors at band 13 in deep convective zones results in low temperatures of observed radiances inside the core of cyclone (upto 70-80 K). Underestimation was observed using the mie-sphere, sector snowflake and six-bullet rosette shapes. Though the overall pattern and location of convective clouds near the eye of cyclone matched closely with the observations, Tb inside the core can be found to vary with hydrometeor shapes and estimates. This may be attributed to deficiency of frozen hydrometeors at sub-grid scale in Kain-Fritsch convection scheme (Rysman et al., 2016). A study by Wu et al., (2015) found that frozen hydrometeors are underestimated in WRF simulations by all convective parametrization schemes over central and eastern pacific region. Rysman et al., (2016) estimate the underestimation in WRF simulations by a factor of 5 using airborne radar in Mediterranean region.

The Figure 4 shows distribution of FG departures in mie-spheres and DDA shapes for all the case study events. A negative departure occurs when the RTToV model is unable to produce realistic representations owing to cloud and precipitation. Within DDA shapes, the pdf curve is found to follow a symmetric distribution. The error is spread equally in both directions due to random forecast errors from first-guess and observations. In case of mie-spheres, the shift towards large negative departures indicates the presence of bias in cloudy region. This is because of insufficient scattering by mie-spheres at band 13 (Geer, 2013). Results show that DDA simulations provide a better realistic scattering in all-sky conditions when FG departures are symmetrical in nature.

3.2 Determination of observation errros with cloud amount

The standard deviations of FG departures in clear-sky assimilation are referred to as observation errors. The observation errors in all-sky radiance assimilation for microwave observations are generally computed from symmetric error models (Geer and Bauer, 2011). Error models are a function of cloud amount predictor at 37 GHz. In the present study, the observed/simulated cloud amounts have been computed from observed/simulated radiances in clear and all-sky conditions.

$$C_{37} = 1 - PD_{37}; \tag{2}$$

$$PD_{37} = \frac{Tb_v - Tb_h}{Tb_v^{clr} - Tb_h^{clr}} \approx \tau_{cloudy}^2 \tag{3}$$

Where, Tb_v & Tb_h are the vertically and horizontal polarised radiances in cloudy condition; Tb_v^{clr} and Tb_h^{clr} are the vertically and horizontal polarized radiances in clear sky condition. PD_{37} is the normalized polarization differences approximately equal to square of transmittance in cloudy region (Petty, 1994). A clear and cloud sky is represented using a PD_{37} of 1 and 0 respectively. For easy interpretation, we preferred cloud amount (C_{37}) which varies from 0 to 1 for the same representation. As the quantities of C_{37obs} and C_{37sim} are affected with sampling error (Geer and Bauer, 2011), their average is considered as the average cloud amount C_{37avg}.

Figure 5 shows the SD_{cloud} curve at band 13 using the C_{37avg} on x-axis in a bin range of 0.05. At C_{37avg}~0, both observations and first-guess are free from clouds (i.e. clear-sky condition). As the C_{37avg} increases, the error is found to initially increase linearly and attain the maxima at C_{37avg}~ 0.48 in all the meteorological events after which the error starts declining to the maximum cloud amount ($C_{37avg} = 1$). The sudden peak at C_{37avg}~0.8 observed in hudhud and vardah cyclones was due to poor representation of Tb at higher frequency using DDA sector snowflake shape in heavy clouds that causes large error.

In symmetric error model, the SD_{cloud} curve was piecewise linearly transformed as a function of C_{37avg} (Geer and Bauer, 2011) (eq. 4).

$$SD_{cloud}\left(C_{37avg}\right) = \begin{array}{c} S_{clr} \;\; if \; C_{37avg} \leq C_{clr} \\ s_{clr} + \left(\frac{S_{cld}-S_{clr}}{C_{cld}-C_{clr}}\right)\left(C_{37avg} - C_{clr}\right) \;\; if \; C_{clr} < C_{37avg} < C_{cld} \\ S_{cld} \;\; if \;\; C_{37avg} \geq C_{cld} \end{array} \quad (4)$$

Here, S_{clr} is the minimum SD_{cloud} defined by the threshold C_{clr} in clear-sky region, whereas S_{cld} is maximum SD_{cloud} in strongly dominating clouds and precipitation region as defined by C_{cld} threshold. These parameters for each cyclone event at band 13 were summarized in Table 2.

3.3 Evaluation of normalized FG departures

The bandwidth of FG departures are very high (Figure 4) and finding a symmetric bias in absolute FG departure is not feasible. Hence, FG departures are normalized with SD_{cloud} (eq. 4) at band 13. The pdf of normalized FG departures were compared with Gaussian for all the deep convective events (Figure 6). From Figure 6, it can be seen that, the normalized FG departure curves follow symmetric distribution but its peak was too high with smaller errors. The main advantage of symmetric error model is to assign large errors in cloudy conditions without causing difficulty in all-sky assimilation.

3.4 Quality Control (QC)

Figure 7 (a), (b) and (c) shows the distribution between observed and simulated Tb using binned scatter plots in 1.0 K by 1.0 K bin for hudhud, vardah and kyant cyclone respectively. Samples found to be outside the range of 100-300 K and bins containing less than or equal to 1 sample were removed from the analysis. The simulated warmer Tb (>240 K) was in good agreement with the observations but samples containing low values of Tb (<240 K) were either from first-guess or from observations having large FG departures. Because of partially random distribution of deep convective clouds, there is a large uncerantity in the prediction of exact location of convective clouds in the model causes the large diagreement (Harnisch et al., 2016). Geer and Bauer, (2011) proposed quality control (QC) method in operational all-sky microwave radiance assimilation to eliminate the large FG departures due to cloud mis-location and instrumental errors, however, their study has not considered the observations wherein normalized FG departures are greater than $\pm$ 2.5 K.

For the present study at band 13, threshold limits cannot be decided using the normalized FG departures. Hence, we performed QC by removing 2.5% samples from both sides of the tail of normalized FG departures. Samples after QC are shown in Figure 7 (d), (e) and (f) and dashed line represent the window of FG departure at 0, ± 10 and $\pm 30\ K$. The low Tb samples removed after QC reduces the variability of FG departure and hence improves the symmetry. Mostly cloudy samples were lie in the error range of $\pm 30\ K$. Results has shown the improvement in correlation coefficient after QC. This method also eliminates the negative departures linked with deep convective events. Figure 8 shows the convective clouds on 10th December 2016 at 03 UTC wherein plots (a), (b) and (c) represent the observed and simulated Tb before and after QC respectively. The cloud information remains preserved after the QC.

3.5 Measure of goodness of fit

Accurate simulation of deep convective events at 183 GHz are challenging due to difficulty in modelling of scattering effects from frozen hydrometeors (Geer and Baordo, 2014; Guerbette et al., 2016). This section measures the goodness of fit between observed and simulated radiances using four widely used DDA shapes. It is common practice to use chi-squared or K-S test to statistically measure the discrepancy between two distributions. Geer and Baordo,(2014) proposed an 'h-statistics' (eq. 5) for smaller samples arranged into number of bins. The value of h could reach infinite if no samples be present in the bin. This study assigns such bins to 0.1 value.

$$h = \frac{\left(\sum_{bins}\left|log\frac{\#\,simulated}{\#\,observ\,ation}\right|\right)}{total\ no\ of\ bins} \tag{5}$$

Here, the bin size is 2.5 K and # denote the numbers.

Atmos. Meas. Tech. Discuss., https://doi.org/10.5194/amt-2018-319
Manuscript under review for journal Atmos. Meas. Tech.
Discussion started: 6 November 2018

Atmospheric Measurement Techniques Discussions
Open Access

The Figure 9 (a), (b) and (c) shows the $log\frac{\#\,simulated}{\#\,observation}$ in y-axis for the case study events that lie within the range of 100-280 K Tb in x-axis for all DDA shapes. In the 100-200 K bins, block column and thin-plate have a positive log ratio which means low Tb occurs extensively due to excessive scattering from clouds while six-bullet rosette and sector snowflake with negative log ratio shows very less or no existence of Tb in this range because of insufficient scattering in heavy cloud and precipitation regions. However, in 200-280 K bins, the log ratio closely lies near to zero and overall good agreement is observed between the observed and simulated Tb. The analysis of DDA shapes shows that thinplate has less peak from 0 to either positive or negative side in all the cases. The h-statistics value for each shape is given in Table 3. Less the number, more will be the similarity. Thin-plate have lowest h-value.

Figure 9 (d) shows the skewness of FG departure for all convective events for each DDA shapes. Large negative or positive value indicate skew towards left or right from normal distribution curve. Combining h-statistics and skewness, thin plate show optimum results among all DDA shapes over Bay of Bengal at band 13. This result is in accordance with the study by Rysman et al., (2016) which shows that thin plate perform best in simulation of all-sky radiances of Advanced Microwave Sounding Unit (AMSU)-B sounding channels in Mediterranean region. Guerbette et al., (2016) observed the best simulations of all-sky SAPHIR radiances with block column shape over Indian Ocean at 183 ± 7 GHz.

3.6 Sensitive to ERA-5 reanalysis datasets

Simulated Tb using ERA-I datasets were compared with ERA-5 (31 km; 3 hr) simulation for all cases. Figure 10 shows the spatial distribution of observed and simulated Tb using DDA thinplate shape for convective clouds at (a, b, c) 10th October 2014-18 UTC (hudhud), (d, e, f) 8th December 2016-15 UTC (vardah) and (g, h, i) 22nd October 2016-18 UTC (kyant). It was observed that the location of clouds and their intensity with ERA-5 datasets was much similar to observations and clear mis-match in distribution of clouds was shown with ERA-I datasets.

The observed and simulated Tb is represented using box-plots and histogram in Figure 11 (a) and (b). The total number of samples are 2445 and correlation coefficient has improved drastically from 0.04 (ERA-I) to 0.52 (ERA-5). The ERA-I simulations have large variability of low Tb due

Atmos. Meas. Tech. Discuss., https://doi.org/10.5194/amt-2018-319
Manuscript under review for journal Atmos. Meas. Tech.
Discussion started: 6 November 2018

to excess scattering from clouds and also decreases the median value. Overall results state that ERA-5 improves the displacement of cloud location, pattern and intensity.

4 Summary and Conclusions

The present study evaluates the simulation of all-sky microwave radiances of GPM/GMI using Weather Research Forecast (WRF) and RTTOV-SCATT (v12.1) radiative transfer model. GMI observations at water vapour sounding channel (183 $\pm$ 7 GHz-V) has been considered and spatially averaged over model resolution. This study has been conducted for three tropical cyclones (Hudhud : 07th -14th Oct. 2014; Vardah: 21st -29th Oct. 2016 and Kyant: 06th -12th Dec. 2016) at 3-h interval and 15 horizontal resolution over Bay of Bengal (BOB) region. In the present study, four recognized DDA shapes (sector snowflake, block column, thin plate and six-bullet rosette) were considered for simulation of brightness temperature (Tb). Results show that simulations using mie-spheres produces bias in cloudy region due to inadequate scattering at 183 $\pm$ 7 GHz while all DDA shapes have significant scattering at higher frequency (Geer and Baordo, 2014) .

We evaluate the cloud effect on FG departures from DDA sector snowflake simulations using symmetric error model. The probability distribution function of normalized FG departures are found to be symmetric. The results show that cloudy samples can offer potential to be assimilated in all-sky radiance assimilation experiments.

The present study also conducted the statistical measures to evaluate the performance of DDA shapes for radiance simulation. The h-statistics is performed to measure the consistency between observed and simulated distributions. We also used skewness, the most suitable parameter in large errors situations (Wilks, 2006). This study observed that thinplate simulates all-sky microwave radiances consistently with observations over BOB region. Our finding resonate with Rysman et al., (2016) over mediterranean region at 183 $\pm$ 7 GHz. In our simulations, we consider only DDA shapes for snow, however in reality there are also high density particles such as hail, aggreagate and graupel hydrometeors which produces very low brightness temperature (Figure 1). Further efforts should be made to include varieties of frozen hydrometeros in RTTOV model. Another improvement can be done in RTTOV-SCATT model to allow multiple DDA shapes of frozen hydrometerors at a time.

Atmos. Meas. Tech. Discuss., https://doi.org/10.5194/amt-2018-319
Manuscript under review for journal Atmos. Meas. Tech.
Discussion started: 6 November 2018

In the present study, simulation of all-sky GMI radiances is carried out with ERA-1 and ERA-5 reanalysis datasets using thinplate shape. Results show improvement in cloud location and intensity near the core when using ERA-5 compared to ERA-I datasets. This can be attributed to the higher spatial and temporal resolution of ERA-5 datasets which when used in WRF model improved the forecast of cloud and precipitation. The initial results using ERA-5 datasets are encouraging and will be a part of ongiong work on radiance simulations. Future work will be focussed on all-sky GMI radiance assimilation in WRF model at higher frequencies for short range forecast over indian region.

Acknowledgement

This work was supported by the Indian Institute of Technology (I.I.T) Bombay, Powai under the Project 15IRCCSG016. We are thankful to the NCAR for the WRF model. The first author would like to thank Dr. James Hocking, Met Office, UK for initial help related to RTTOV-SCATT Model. We would like to thank the Goddard Distributed Active Archive Center (GES DISC DAAC) for providing the GMI radiances and are free available at https://mirador.gsfc.nasa.gov/. The ERA-I and ERA-5 datasets are obtained from http://rda.ucar.edu/datasets/ds627.0 and https://rda.ucar.edu/datasets/ds630.0/ respectively.

References

De Angelis, F., Cimini, D., Löhnert, U., Caumont, O., Haefele, A., Pospichal, B., Martinet, P., Navas-Guzmán, F., Klein-Baltink, H., Dupont, J.-C. and Hocking, J.: Long term Observations minus Background monitoring of ground-based microwave radiometer network. Part 1: Brightness Temperatures, Atmos. Meas. Tech. Discuss., 1–24, doi:10.5194/amt-2017-112, 2017.

Bennartz, R. and Bauer, P.: Sensitivity of microwave radiances at 85-183 GHz to precipitating ice particles, Radio Sci., 38(4), n/a-n/a, doi:10.1029/2002RS002626, 2003.

Dudhia, J.: Numerical Study of Convection Observed during the Winter Monsoon Experiment Using a Mesoscale Two-Dimensional Model, J. Atmos. Sci., 46(20), 3077–3107, doi:10.1175/1520-0469(1989)046<3077:NSOCOD>2.0.CO;2, 1989.

Errico, R. M., Bauer, P. and Mahfouf, J.-F.: Issues Regarding the Assimilation of Cloud and Precipitation Data, J. Atmos. Sci., 64(11), 3785–3798, doi:10.1175/2006JAS2044.1, 2007.

Atmos. Meas. Tech. Discuss., https://doi.org/10.5194/amt-2018-319
Manuscript under review for journal Atmos. Meas. Tech.
Discussion started: 6 November 2018

Atmospheric Measurement Techniques
Discussions

Field, P. R., Heymsfield, A. J. and Bansemer, A.: Snow Size Distribution Parameterization for Midlatitude and Tropical Ice Clouds, J. Atmos. Sci., 64(12), 4346–4365, doi:10.1175/2007JAS2344.1, 2007.

Fowler, A. and Van Leeuwen, P. J.: Observation impact in data assimilation: The effect of non-gaussian observation error, Tellus, Ser. A Dyn. Meteorol. Oceanogr., 65, doi:10.3402/tellusa.v65i0.20035, 2013.

Geer, A. J.: All-sky assimilation: better snow-scattering radiative transfer and addition of SSMIS humidity sounding channels., 2013.

Geer, A. J. and Baordo, F.: Improved scattering radiative transfer for frozen hydrometeors at microwave frequencies, Atmos. Meas. Tech., 7(6), 1839–1860, doi:10.5194/amt-7-1839-2014, 2014.

Geer, A. J. and Bauer, P.: Observation errors in all-sky data assimilation, Q. J. R. Meteorol. Soc., 137(661), 2024–2037, doi:10.1002/qj.830, 2011.

Geer, A. J., Bauer, P. and O'Dell, C. W.: A revised cloud overlap scheme for fast microwave radiative transfer in rain and cloud, J. Appl. Meteorol. Climatol., 48(11), 2257–2270, doi:10.1175/2009JAMC2170.1, 2009.

Guerbette, J., Mahfouf, J. F. and Plu, M.: Towards the assimilation of all-sky microwave radiances from the SAPHIR humidity sounder in a limited area NWP model over tropical regions, Tellus, Ser. A Dyn. Meteorol. Oceanogr., 68(March), doi:10.3402/tellusa.v68.28620, 2016.

Harnisch, F., Weissmann, M. and Periáñez: Error model for the assimilation of cloud-affected infrared satellite observations in an ensemble data assimilation system, Q. J. R. Meteorol. Soc., 142(697), 1797–1808, doi:10.1002/qj.2776, 2016.

Hocking, J., Rayer, P., Rundle, D., Saunders, R., Matricardi, M., Geer, A., Brunel, P. and Vidot, J.: “RTTOV v12 Users Guide”, NWCSAF report. EUMETSAT: Darmstadt, Germany., 2017.

Hong, G., Heygster, G., Miao, J. and Kunzi, K.: Detection of tropical deep convective clouds from AMSU-B water vapor channels measurements, J. Geophys. Res. D Atmos., 110(5), 1–15, doi:10.1029/2004JD004949, 2005.

Atmos. Meas. Tech. Discuss., https://doi.org/10.5194/amt-2018-319
Manuscript under review for journal Atmos. Meas. Tech.
Discussion started: 6 November 2018

Hong, S.-Y., Noh, Y. and Dudhia, J.: A New Vertical Diffusion Package with an Explicit Treatment of Entrainment Processes, Mon. Weather Rev., 134(9), 2318–2341, doi:10.1175/MWR3199.1, 2006.

Hong, S. and Lim, J.: The WRF single-moment 6-class microphysics scheme (WSM6), J. Korean Meteorol. Soc., 42(2), 129–151 [online] Available from: http://www.mmm.ucar.edu/wrf/users/docs/WSM6-hong_and_lim_JKMS.pdf%5Cnhttp://search.koreanstudies.net/journal/thesis_name.asp?tname=kiss2002&key=2525908, 2006.

Hou, A. Y., Kakar, R. K., Neeck, S., Azarbarzin, A. A., Kummerow, C. D., Kojima, M., Oki, R., Nakamura, K. and Iguchi, T.: The global precipitation measurement mission, Bull. Am. Meteorol. Soc., 95(5), 701–722, doi:10.1175/BAMS-D-13-00164.1, 2014.

Islam, T., Srivastava, P. K., Petropoulos, G. P. and Singh, S. K.: Reduced major axis approach for correcting GPM/GMI radiometric biases to coincide with radiative transfer simulation, J. Quant. Spectrosc. Radiat. Transf., 168, 40–45, doi:10.1016/j.jqsrt.2015.08.016, 2016.

JAXA: GCOM-W1 Shizuku Data Users Handbook., 2013.

Joseph, J. H., Wiscombe, W. J. and Weinman, J. a: The delta-Eddington approximation for radiative flux transfer, J. Atmos. Sci., 33, 2452, doi:10.1175/1520-0469(1976)033<2452:TDEAFR>2.0.CO;2, 1976.

Kain, J. S.: The Kain–Fritsch Convective Parameterization: An Update, J. Appl. Meteorol., 43(1), 170–181, doi:10.1175/1520-0450(2004)043<0170:TKCPAU>2.0.CO;2, 2004.

Kawanishi, T., Sezai, T., Ito, Y., Imaoka, K., Takeshima, T., Ishido, Y., Shibata, A., Miura, M., Inahata, H. and Spencer, R. W.: The Advanced Microwave Scanning Radiometer for the Earth observing system (AMSR-E), NASDA's contribution to the EOS for global energy and water cycle studies, IEEE Trans. Geosci. Remote Sens., 41(2 PART 1), 184–193, doi:10.1109/TGRS.2002.808331, 2003.

Kazumori, M. and English, S. J.: Use of the ocean surface wind direction signal in microwave radiance assimilation, Q. J. R. Meteorol. Soc., 141(689), 1354–1375, doi:10.1002/qj.2445, 2015.

Kazumori, M., Geer, A. J. and English, S. J.: Effects of all-sky assimilation of GCOM-W1/AMSR2

Atmos. Meas. Tech. Discuss., https://doi.org/10.5194/amt-2018-319
Manuscript under review for journal Atmos. Meas. Tech.
Discussion started: 6 November 2018

radiances in the ECMWF system., 2014.

Kumar, P., Kishtawal, C. M. and Pal, P. K.: Impact of satellite rainfall assimilation on Weather Research and Forecasting model predictions over the Indian region, J. Geophys. Res. Atmos., 1–15, doi:10.1002/2013JD020005.Received, 2014.

Kummerow, C., Barnes, W., Kozu, T., Shiue, J. and Simpson, J.: The Tropical Rainfall Measuring Mission (TRMM) sensor package, J. Atmos. Ocean. Technol., 15(3), 809–817, doi:10.1175/1520-0426(1998)015<0809:TTRMMT>2.0.CO;2, 1998.

Kunkee, D. B., Poe, G. A., Boucher, D. J., Swadley, S. D., Hong, Y., Wessel, J. E. and Uliana, E. A.: Design and evaluation of the first special sensor microwave imager/sounder, IEEE Trans. Geosci. Remote Sens., 46(4), 863–883, doi:10.1109/TGRS.2008.917980, 2008.

Laviola, S. and Levizzani, V.: The 183-WSL fast rain rate retrieval algorithm. Part I: Retrieval design., Atmos. Res., 99(3–4), 443–461, doi:10.1016/j.atmosres.2010.11.013, 2011.

Lean, P., Geer, A. and Lonitz, K.: Assimilation of Global Precipitation Mission (GPM) Microwave Imager (GMI) in all-sky conditions., 2017.

Liu, G.: A database of microwave single-scattering properties for nonspherical ice particles, Bull. Am. Meteorol. Soc., 89(10), 1563–1570, doi:10.1175/2008BAMS2486.1, 2008.

Malardel, S., Wedi, N., Deconinck, W., Diamantakis, M., Kuhnlein, C., Mozdzynski, G., Hamrud, M. and Smolarkiewicz, P.: A new grid for the IFS., 2015.

Mlawer, E. J., Taubman, S. J., Brown, P. D., Iacono, M. J. and Clough, S. A.: Radiative transfer for inhomogeneous atmospheres: RRTM, a validated correlated-k model for the longwave, J. Geophys. Res. Atmos., 102(D14), 16663–16682, doi:10.1029/97JD00237, 1997.

Okamoto, K.: Evaluation of IR radiance simulation for all-sky assimilation of Himawari-8/AHI in a mesoscale NWP system, Q. J. R. Meteorol. Soc., 143(704), 1517–1527, doi:10.1002/qj.3022, 2017.

Okamoto, K., McNally, A. P. and Bell, W.: Progress towards the assimilation of all-sky infrared radiances: An evaluation of cloud effects, Q. J. R. Meteorol. Soc., 140(682), 1603–1614, doi:10.1002/qj.2242, 2014.

Otkin, J. A.: Assimilation of water vapor sensitive infrared brightness temperature observations during a high impact weather event, J. Geophys. Res. Atmos., 117(19), 1–16, doi:10.1029/2012JD017568, 2012.

Petty, G. W.: Physical retrievals of over-ocean rain rate from multichannel microwave imagery. Part I: Theoretical characteristics of normalized polarization and scattering indices, Meteorol. Atmos. Phys., 54(1–4), 79–99, doi:10.1007/BF01030053, 1994.

Routray, A., Mohanty, U. C., Osuri, K. K., Kar, S. C. and Niyogi, D.: Impact of Satellite Radiance Data on Simulations of Bay of Bengal Tropical Cyclones Using the WRF-3DVAR Modeling System, IEEE Trans. Geosci. Remote Sens., 54(4), 2285–2303, doi:10.1109/TGRS.2015.2498971, 2016.

Rysman, J.-F., Berthou, S., Claud, C., Drobinski, P., Chaboureau, J.-P. and Delanoë, J.: Potential of microwave observations for the evaluation of rainfall and convection in a regional climate model in the frame of HyMeX and MED-CORDEX, Clim. Dyn., doi:10.1007/s00382-016-3203-7, 2016.

Saunders, R., Hocking, J., Rundle, D., Rayer, P., Havemann, S., Matricardi, M., Geer, A., Lupu, C., Brunel, P. and Vidot, J.: "RTTOV-12 science and validation report." [online] Available from: https://www.nwpsaf.eu/site/download/documentation/rtm/docs_rttov12/rttov12_svr.pdf?d7478d &d7478d, 2017.

Saunders, R. W., Blackmore, T. a, Candy, B., Francis, P. N., Hewison, T. J. and Member, S.: Monitoring Satellite Radiance Biases Using NWP Models, IEEE Trans. Geosci. Remote Sens., 51(3), 1124–1138, 2013.

Shastri, H., Barik, B., Ghosh, S., Venkataraman, C. and Sadavarte, P.: Flip flop of Day-night and Summer-Winter Surface Urban Heat Island Intensity in India, Sci. Rep., 7(January), 1–8, doi:10.1038/srep40178, 2017.

Simmons, A. J., Uppala, S. M., Dee, D. P. and Kobayashi, S.: ERA-Interim: New ECMWF reanalysis products from 1989 onwards, ECMWF Newsl., 110(110), 25–35, doi:ECMWF Newsletter n.110, 2007.

Singh, R., Ojha, S. P., Kishtawal, C. M., Pal, P. K. and Kiran Kumar, A. S.: Impact of the assimilation of INSAT-3D radiances on short-range weather forecasts, Q. J. R. Meteorol. Soc., 142(694), 120–131, doi:10.1002/qj.2636, 2016.

Skamarock, W. C., Klemp, J. B., Dudhi, J., Gill, D. O., Barker, D. M., Duda, M. G., Huang, X.-Y., Wang, W. and Powers, J. G.: A Description of the Advanced Research WRF Version 3, Tech. Rep., (June), 113, doi:10.5065/D6DZ069T, 2008.

Skofronick-Jackson, G. M. and Wang, J. R.: The estimation of hydrometeor profiles from wideband microwave observations, J. Appl. Meteorol., 39(10), 1645–1656, doi:10.1175/1520-0450-39.10.1645, 2000.

Tewari, M., Chen, F., Wang, W., Dudhia, J., LeMone, M. A., Mitchell, K., Ek, M., Gayno, G., Wegiel, J. and Cuenca, R. H.: Implementation and verification of the unified noah land surface model in the WRF model, Bull. Am. Meteorol. Soc., 2165–2170, doi:10.1007/s11269-013-0452-7, 2004.

Wilks, D. S.: Statistical Methods in the Atmospheric Sciences, Elsevier., 2006.

Wu, L., Li, J. L. F., Pi, C. J., Yu, J. Y. and Chen, J. P.: An observationally based evaluation of WRF seasonal simulations over the Central and Eastern Pacific, J. Geophys. Res., 120(20), 10,664-10,680, doi:10.1002/2015JD023561, 2015.

Atmospheric Measurement Techniques Discussions

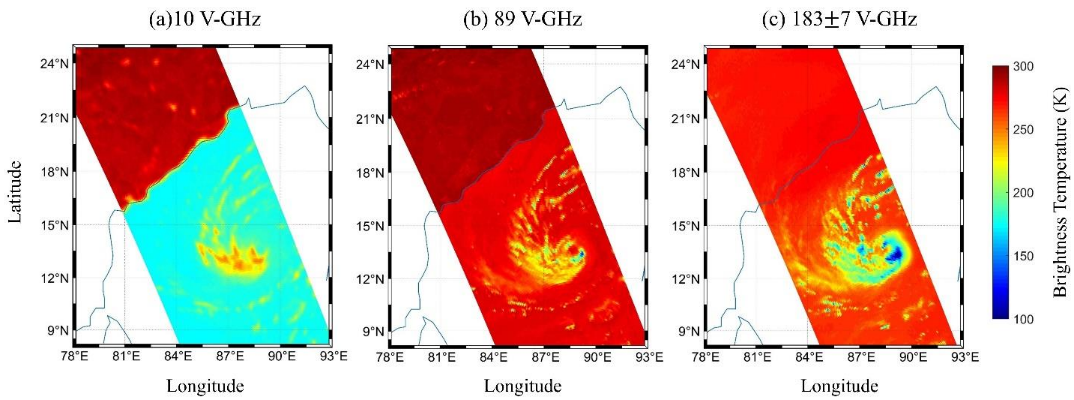

Figure 1: Brightness Temperature from GPM GMI for (a) 10 V-GHz, (b) 89 V-GHz and (c) 183 ± 7 GHz for hudhud cyclone event on 9th October 2018 at 06 UTC. The frozen hydrometeors information are more enhanced at 183 ± 7 GHz frequency.

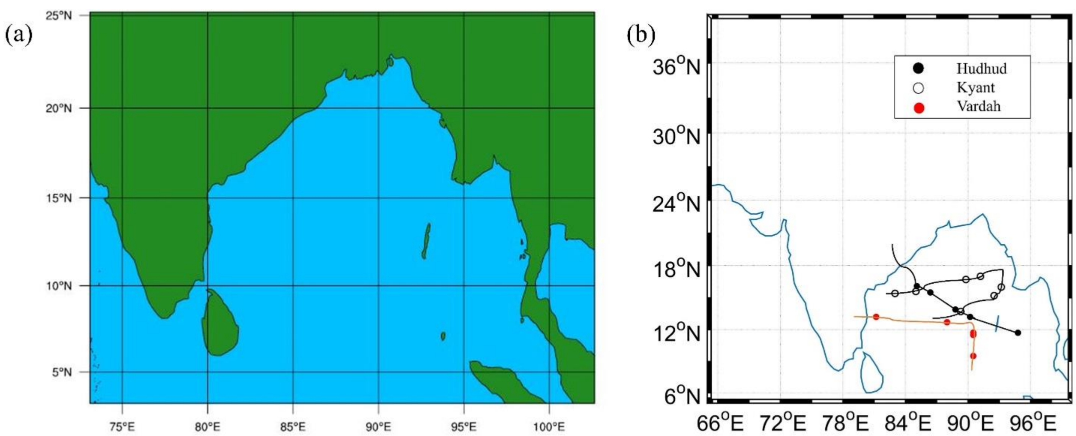

Figure 2: (a) Single WRF domain used for the simulation of three Tropical cyclones (Hudhud, Vardah and Kyant) over Bay of Bengal and (b) shows the track of cyclones and dot point represent the availability of GMI observations near the eye of cyclone

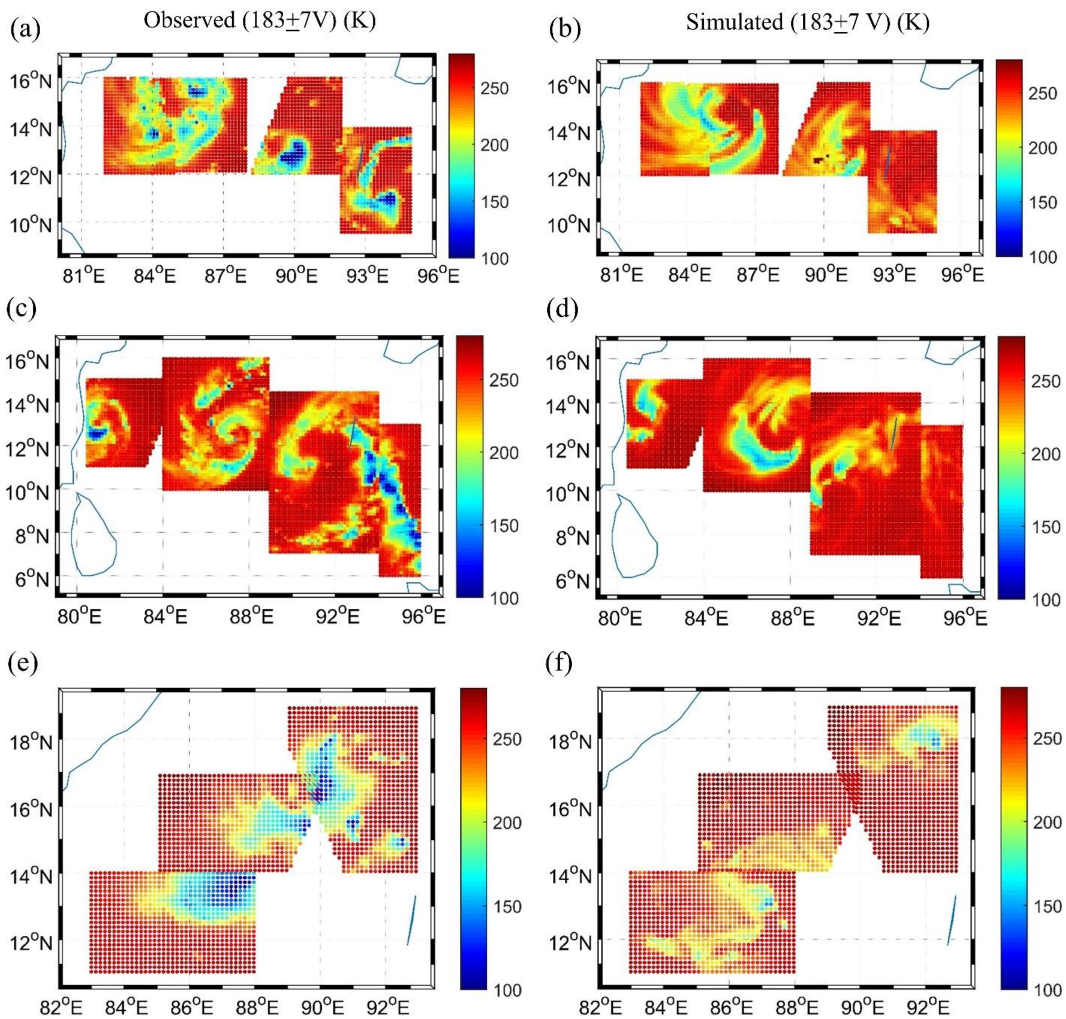

Figure 3: Spatial distribution of (a, c and e) GMI observed brightness temperature (Tb) and (b, d and f) simulated Tb with default DDA sector shape at band 13 for hudhud, vardah and kyant cyclone respectively.

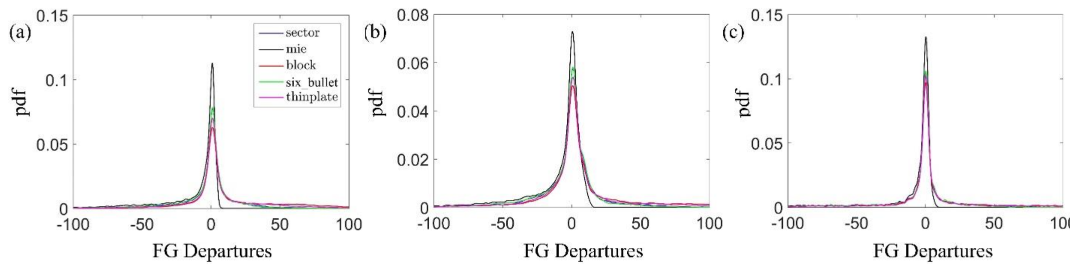

Figure 4: Probability distribution function (PDF) of observed-background (FG departures) with mie-spheres and DDA shapes for (a) hudhud, (b) vardah and (c) kyant cyclone.

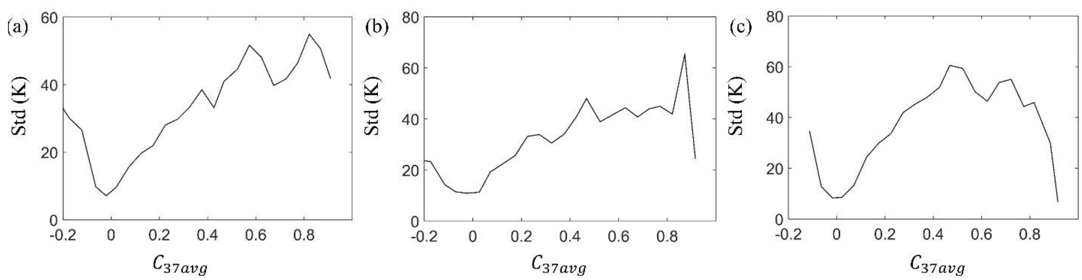

Figure 5: Standard deviation (SD_{cloud}) curve with respect to average cloud amount at band 13 for (a) hudhud, (b) vardah and (c) kyant cyclone. The cloud amount bin is 0.05 at x-axis.

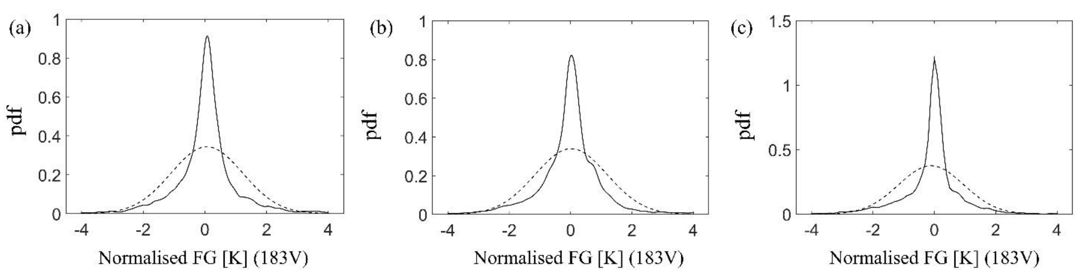

Figure 6: Probability distribution function (PDF) of FG departure normalized by standard deviation as function of average cloud amount for (a) hudhud (b) vardah and (c) kyant cyclone at band 13. The dotted curve represent the Gaussian curve.

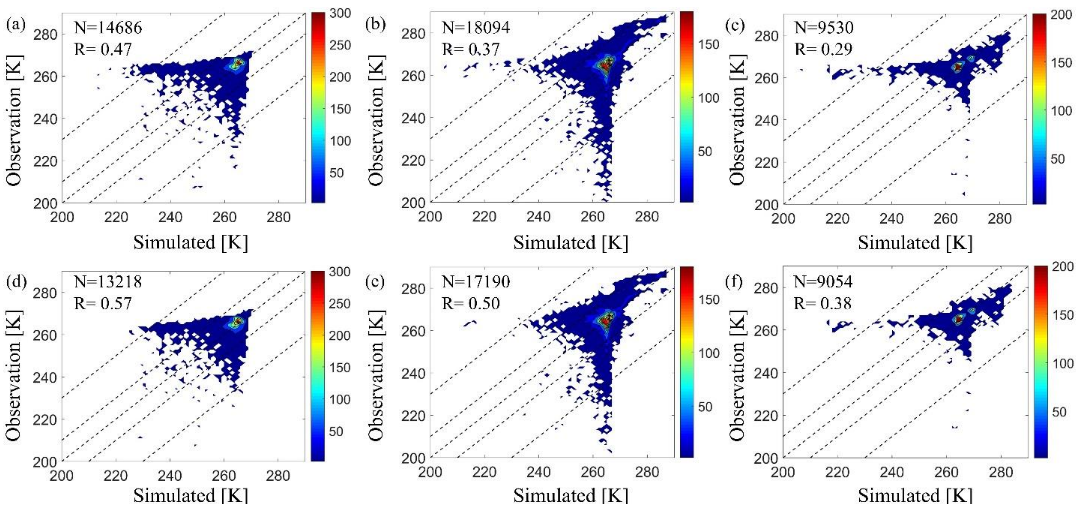

Figure 7: Binned scatter plots of background and simulated brightness temperature at band 13 for (a, d) hudhud, (b, e) vardah and (c, f) kyant cyclone before and after Quality Control (QC). The samples are counted in 1.0 K by 1.0 K. The colorbar refers to the density in each bin. Dashed line represent the FG departure at 0, ± 10 *and* ± 30 *K*.

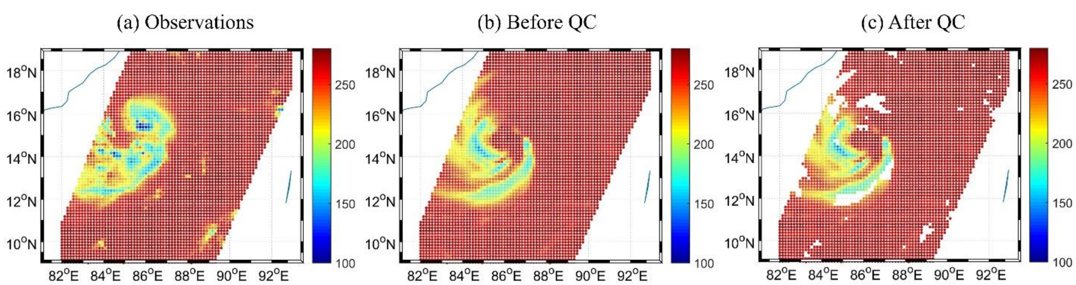

Figure 8: shows the convective events at 10th October 2014:18 UTC represents (a) GMI observations, (b) Simulated Tb before QC, (c) after QC. The pixels of high FG departures due to mis-match of location were removed.

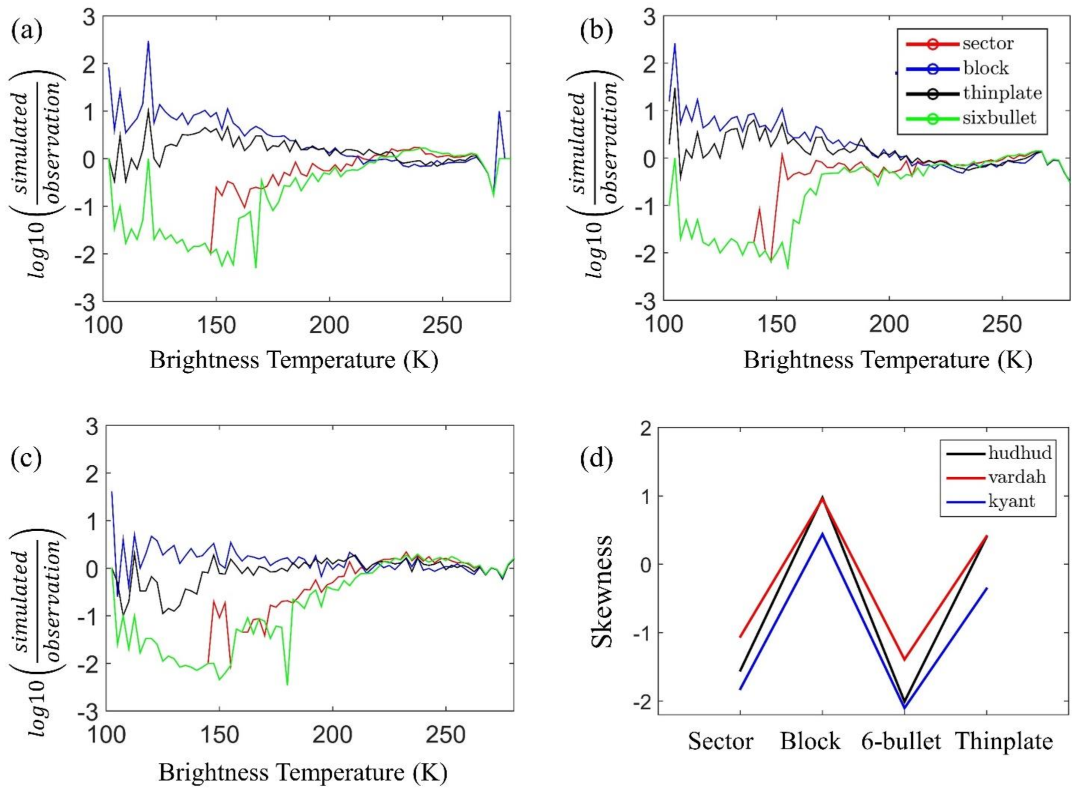

Figure 9: Measure of goodness of fit. The log of the ratio of histograms (simulation divided by the observation) for four different DDA shapes over (a) hudhud, (b) vardah and (c) kyant cyclone. The bin size is 2.5 K. (d) represents the skewness of FG departures. Thinplate performs the best results over Bay of Bengal.

Atmos. Meas. Tech. Discuss., https://doi.org/10.5194/amt-2018-319
Manuscript under review for journal Atmos. Meas. Tech.
Discussion started: 6 November 2018

Atmospheric Measurement Techniques
Discussions

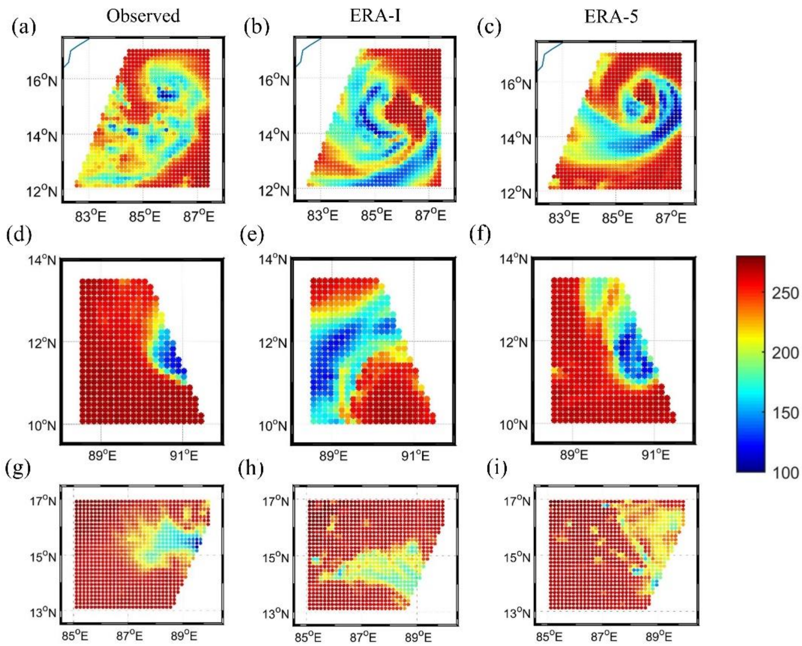

Figure 10: Observed and Simulated Tb with ERA-I and ERA-5 reanalysis datasets for a day event (a, b, c) 10th October 2014, 18 UTC (hudhud cyclone); (d, e, f) 8th December 2016, 15 UTC (vardah cyclone) and (g, h, i) 22nd October 2016, 18 UTC (kyant cyclone).

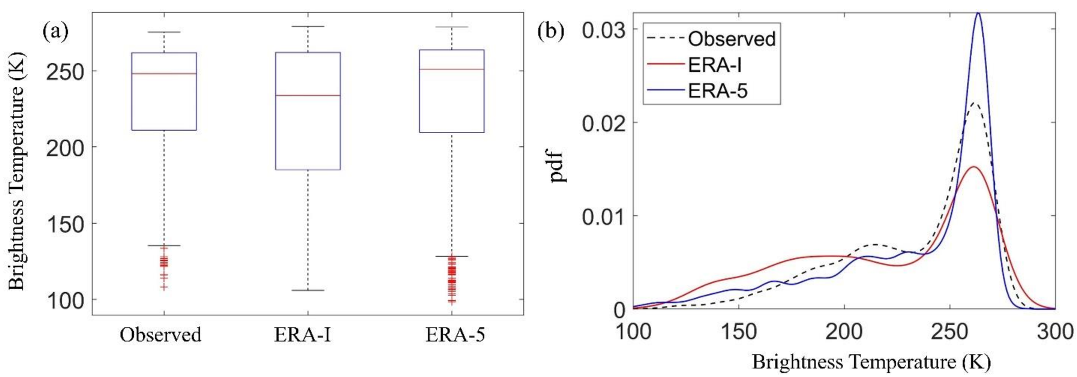

Figure 11: (a) Boxplot of observed and Simulated Tb with ERA-I and ERA-5 reanalysis datasets. The 50 percentile of ERA-I simulations is larger than observed data due to excess scattering from the clouds. (b) Histogram of observed and simulated brightness temperature. ERA-5 simulations have similarity with observed data.

Atmos. Meas. Tech. Discuss., https://doi.org/10.5194/amt-2018-319
Manuscript under review for journal Atmos. Meas. Tech.
Discussion started: 6 November 2018

Table 1. GMI sensor characteristics (Hou et al., 2014)

Channels	Frequency (GHz)	Polarization	Resolution (Km)
1, 2	10.65	V, H	19.4 x 32.2
3,4	18.7	V, H	11.2 x 18.3
5	23.8	V	9.2 x 15.0
6,7	36.5	V, H	8.6 x 15.0
8,9	89.0	V, H	4.4 x 7.3
10,11	166	V, H	4.4 x 7.3
12	183±3	V	4.4 x 7.3
13	183±7	V	4.4 x 7.3

Table 2. Standard deviation and threshold for identifying clear-sky and cloudy samples at 183 ± 7 V GHz for all tropical cyclones.

	Hudhud	Vardah	Kyant
S_{clr}	9.5977	11.2895	8.9561
S_{cld}	51.6524	47.9787	61.7815
C_{cld}	0.5733	0.4677	0.5218
C_{clr}	0.0209	0.0266	0.0213

Atmos. Meas. Tech. Discuss., https://doi.org/10.5194/amt-2018-319
Manuscript under review for journal Atmos. Meas. Tech.
Discussion started: 6 November 2018

Atmospheric Measurement Techniques
Open Access
Discussions

Table 3. shows the h-value and skewness corresponding to the all meteorological events for different DDA shapes. Thinplate has the least h-value and low skewness in all events.

DDA shapes	Hudhud		Vardah		Kyant	
	h-value	skewness	h-value	skewness	h-value	skewness
Sector	0.6297	-1.5516	0.5477	-1.0571	0.7565	-1.8218
Block	0.4893	0.9733	0.4064	0.9533	0.2522	0.4399
6- bullet	0.8171	-2.0069	0.7028	-1.3925	0.8838	-2.1021
Thinplate	0.2743	0.3982	0.2528	0.4089	0.2397	-0.3575